This is an open access article published under an ACS AuthorChoice License, which permits copying and redistribution of the article or any adaptations for non-commercial purposes.

ACS OMEGA

Article

Cite This: ACS Omega 2019, 4, 2398−2409

http://pubs.acs.org/journal/acsodf

Unveiling the Reaction Mechanism during Li Uptake and Release of Nanosized "$NiFeMnO_4$": Operando X-ray Absorption, X-ray Diffraction, and Pair Distribution Function Investigations

Stefan Permien,[†,⊥] Anna-Lena Hansen,[†] Jonas van Dinter,[†] Sylvio Indris,[‡] Gero Neubüser,[∥] Lorenz Kienle,[∥] Stephen Doyle,[§] Stefan Mangold,[§] and Wolfgang Bensch*[,†]

[†]Institute of Inorganic Chemistry, University of Kiel, Max-Eyth-Straße 2, 24118 Kiel, Germany

[‡]IAM-ESS and [§]ANKA Synchrotron Radiation Facility, Karlsruhe Institute of Technology, P.O. Box 3640, 76021 Karlsruhe, Germany

[∥]Institute for Materials Science, University of Kiel, Kaiserstraße 2, 24143 Kiel, Germany

Supporting Information

ABSTRACT: Here, we report that the trimetallic nanosized oxide $NiFeMnO_4$ consists of a mixture of NiO and a strained cubic spinel phase, which is clearly demonstrated by analysis of the pair distribution function (PDF) and synchrotron X-ray data. Such a finding can easily be overlooked by using only inhouse X-ray powder diffraction, leading to inaccurate assumption of the stoichiometry and oxidation states. Such advanced characterization is essential because a homogeneous distribution of the elements is observed in energy-dispersive X-ray spectroscopy maps, giving no hints for a phase separation. Cycling of the sample against Li delivers a high reversible capacity of ≈840 mAh/g in the 50th cycle. Operando X-ray absorption spectroscopy (XAS) experiments indicate that ≈0.8 Li/fu is consumed without detectable changes of the electronic structure. Increasing amounts of Li, Mn^{3+}, and Fe^{3+} are simultaneously reduced. The disappearance of the pre-edge features in X-ray absorption near-edge spectroscopy indicates movement of these cations from tetrahedral sites to octahedral sites. PDF analysis of the pattern after an uptake of 2 Li/fu evidences that the principal structure can be sufficiently well modeled assuming coexisting NiO, a mixed monoxide, and a small amount of residual spinel phase. Thus, the majority of cations is located on octahedral sites. Furthermore, an improvement of the PDF model is achieved taking into account small amounts of LiOH. The ^{7}Li MAS NMR spectrum of this sample clearly shows the signal of Li in a diamagnetic environment, excluding Li−O−TM bonds. A further increase of the Li content leads to a successive conversion of the cations to nanosized metal particles embedded in a $LiOH/Li_2O$ matrix. Ex situ XAS results indicate that Fe can be reversibly reoxidized to Fe^{3+} during charge whereas Mn does not reach the oxidation state observed in the pristine material. After excessive cycling, reoxidation of metallic Ni is suppressed and contributes to a capacity loss compared with the early discharge/charge cycles.

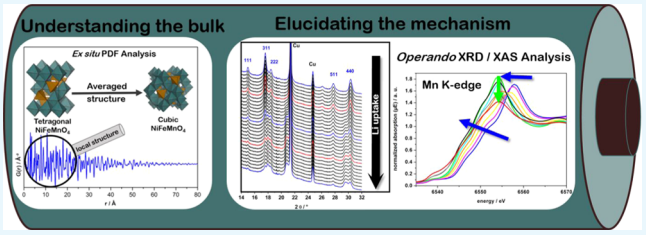

1. INTRODUCTION

Lithium-ion batteries (LIBs) deliver electricity in portable electronic devices.[1−5] Many efforts were undertaken during the last decades, resulting in improvements of the capacity, safety, and cyclability of LIBs.[6,7] In commercial LIBs, Ni- and/or Co-containing oxides are used as cathodes and carbon as anode. During discharge, Li^+ ions are intercalated in the oxidic host material (cathode) and during charge, the ions move into graphitic anode material. The intercalation and deintercalation processes with less than 1 Li/fu being shuttled between the electrodes lead to relatively low specific capacities. This low specific capacity has intensified the research in the field of LIBs, and conversion reactions were identified as a possible alternative reaction mechanism to obtain a high capacity.

A number of transition-metal (TM) oxides were identified as conversion materials that can deliver capacities of more than 1000 mAh/g.[8−12] These materials also fulfill requirements concerning price, abundance, toxicity, and sustainability. Studies of such conversion materials date back to the last century and were mainly performed by Goodenough and colleagues.[13,14] The great success of intercalation LIBs led to a significant decline of the research on conversion electrodes. For several years now, the worldwide debate about renewable energy sources and especially the need for large-scale energy storage devices as well as LIBs with larger capacities has caused a renaissance in this field of battery research.[1,2,8,9,15−20]

In a number of investigations, it was demonstrated that nanoparticles improve the electrochemical performance due to shorter diffusion pathways and packing of the particles, leading

Received: November 23, 2018
Accepted: December 11, 2018
Published: January 31, 2019

Downloaded via DEUTSCHES ELEKTRONEN-SYNCHROTRON on November 11, 2019 at 11:43:08 (UTC).
See https://pubs.acs.org/sharingguidelines for options on how to legitimately share published articles.

to hollow spaces to compensate the volume changes associated with conversion reactions.[21−23]

Although a large number of binary TM oxides were studied in LIB conversion reactions, investigations using spinel oxides with three transition metals are scarce. The two spinel oxides $NiFe_2O_4$ and $NiMn_2O_4$ exhibit high theoretical and experimental reversible capacities as anode materials in LiBs.[20,24−30] $NiFe_2O_4$ crystallizes in an inverse spinel structure ($[A^{III}]_{tet}[B^{II}]_{okt}O_4$−$[Fe^{III}][Ni^{II}Fe^{II}]O_4$), whereas the distribution of the cations is known to be more complex in the case of $NiMn_2O_4$ due to phonon-assisted hopping of charge carriers and disproportionation of Mn^{3+} according to ($[Ni^{II}_{1-y}Mn^{II}_y]$-$i^{II}_yMn^{III}_{2(1-y)}Mn^{IV}_y]O_4$).[31,32] As a consequence of the strong octahedral site preference of Ni^{2+}, this latter spinel phase seems to be less stable and prone to decomposition.[31] Moreover, due to an appreciable amount of the Jahn−Teller ion Mn^{3+} on the B site, Mn^{3+} containing spinels often exhibit a tetragonal distortion and the symmetry is reduced ($Fd\bar{3}m \rightarrow I4_1/amd$). Larson et al. proposed a critical concentration of Mn^{3+} of 58−65% above which a tetragonal symmetry reduction occurs.[29,33−35] This value can be reduced by substituting of Fe^{3+} for Mn^{3+}. The first report about $NiMnFeO_4$ nanoparticles (<100 nm) as anode material showed a reversible capacity of 750 mAh/g after 50 cycles, comparable to the performance of $NiFe_2O_4$ and even better than that of $NiMn_2O_4$.[36]

In the past few years, we investigated the reaction mechanisms of Li uptake and release of nanocrystalline spinels using operando X-ray diffraction (XRD) and operando X-ray absorption spectroscopy (XAS), accompanied by ex situ techniques, like galvanostatic cycling, NMR spectroscopy, cyclovoltammetry, high-resolution transmission electron microscopy (HRTEM), and elemental analysis.[37−42]

The combination of these techniques allowed elucidation of detailed reaction mechanisms on different structural length scales and the changes of the electronic structures. For all materials, we observed formation of a monoxide with a NaCl-type structure after conversion of about 2 Li/fu. From a thermodynamic point of view, the formation of mixed transition-metal monoxides is surprising because for several combinations of metal cations, elevated temperatures are required for their formation.[43] The NaCl-like structure is realized by simultaneous reduction of the M^{3+} cations to M^{2+} and movement of M^{2+} to empty octahedral sites. In addition, O^{2-} anions must be expelled and most probably Li_2O is formed. Increasing the Li content leads to a successive further reduction of the cations to the metallic state (exception: Mg^{2+} in $MgFe_2O_4$ could not be reduced) and after full discharge, metallic nanoparticles are embedded in a Li_2O matrix. During the charge process, the metallic particles are oxidized and amorphous or nanocrystalline oxides are formed.

In situ/operando XRD investigations probe the formation of new crystalline phases on the long-range scale, and the local environment and the changes of the electronic properties can be investigated using in situ/operando XAS experiments.[37−41] Pair distribution function (PDF) analysis allows characterization of nanosized materials from the atomic to the nanometer scale, thus complementing XRD and XAS.[42] The results achieved by such experiments are complemented by ex situ characterizations, thus finally leading to a detailed picture of reaction mechanisms of the complex conversion reactions taking place during Li uptake/release.

In the manuscript, we report on results of our investigations on $NiMnFeO_4$ nanoparticles used as anode material for LiBs. The focus of the study is the clarification of the structural and electronic reaction mechanisms. Therefore, Li uptake/release of $NiMnFeO_4$ was investigated in detail by operando XRD and XAS, ex situ ^{7}Li MAS NMR, XRD, PDF, XAS, and TEM. The electrochemical performance of the material was characterized using galvanostatic cycling and cyclic voltammetry (CV).

2. RESULTS AND DISCUSSION

2.1. Structural Characterization. The X-ray powder pattern of the as-prepared $NiMnFeO_4$ nanoparticles is presented in Figure 1. Although the general appearance of the pattern agrees with that of a typical cubic spinel structure, Rietveld refinement was not satisfactory and pronounced deviations of the relative intensities could be observed. As a second phase, NiO (rock salt structure) was added in the refinement and the refined lattice parameter of a = 4.1675(1) Å is in good agreement with literature data ($a_{ICSD28834}$ = 4.170 Å). In addition, it was necessary to introduce a strain parameter for the spinel phase for adequate modeling the powder pattern (Table S1). From the refinement, the sizes of coherently scattering domains were 17(1) nm for the spinel and 11(1) nm for NiO.

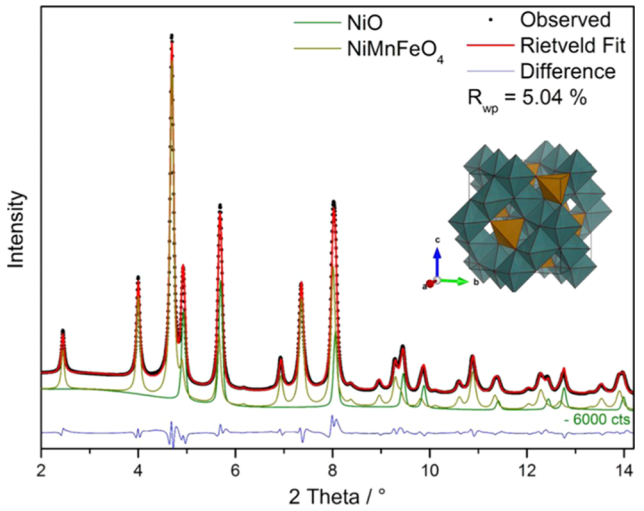

Figure 1. X-ray powder diffraction pattern of $NiMnFeO_4$ nanoparticles (black) with Rietveld Fit (red) and difference calculation (blue) and the calculated pattern of spinel (gold), corresponding to the schematic structure, and NiO (green), both shifted to a lower intensity for the sake of clarity. Measured at beamline P02.1, DESY using 60 keV (λ = 0.2073 Å).

The occurrence of alternating spinel and rock salt domains in solid solutions of rock salt and spinel samples was discussed by Armbruster.[44] In addition, rock salt and defect rock salt-type impurities, i.e., NiO, $Ni_{0.5}Mn_{0.5}O$, or Ni_6MnO_8, were reported several times in these and closely related compounds.[31,45−48] Nevertheless, due to the uniform cation distribution, revealed by TEM-energy-dispersive X-ray (EDX) mapping analysis, it can be assumed that a domain intergrowth as described in ref 33 is more likely than a phase separation.

The amount of NiO was estimated on the basis of Rietveld refinement to be ∼23 wt % (Table S1). Therefore, the stoichiometry of the spinel must deviate from its desired value, and the stoichiometry was determined on the basis of the work by Feltz and Pölzl:[31]

DOI: 10.1021/acsomega.8b03276
ACS Omega 2019, 4, 2398−2409

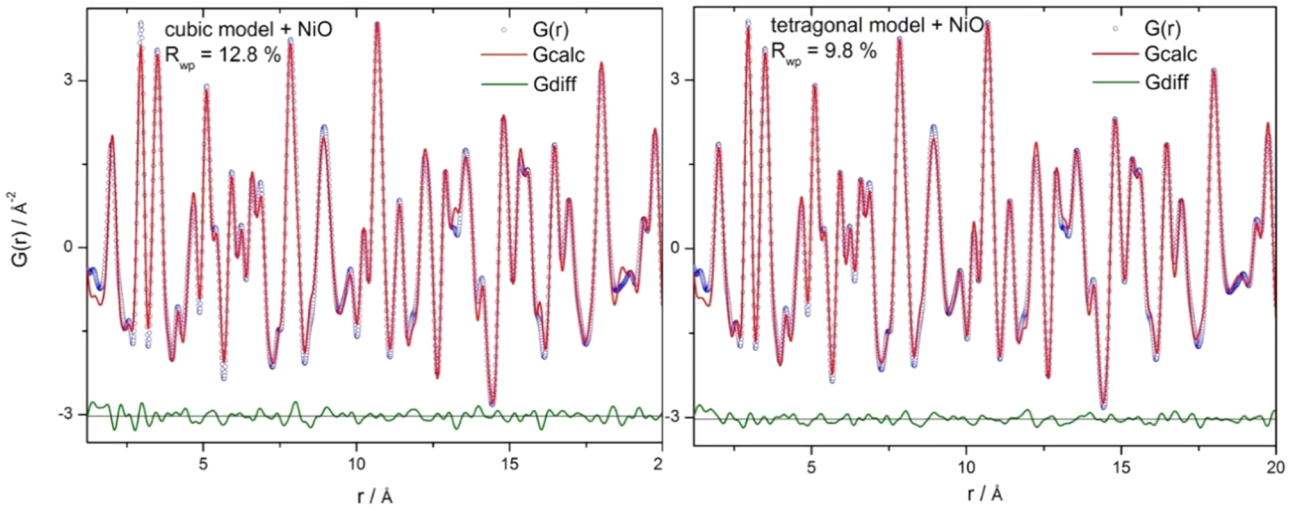

Figure 2. Comparison of two models with PDF obtained from total scattering experiments at beamline P02.1, DESY. The cubic model on the left shows enhanced deviations compared with the tetragonal model on the right. The R_{wp} value determined by a Rietveld-like least square refinement is lower for the tetragonal model, indicating a more suitable description of the local structure.

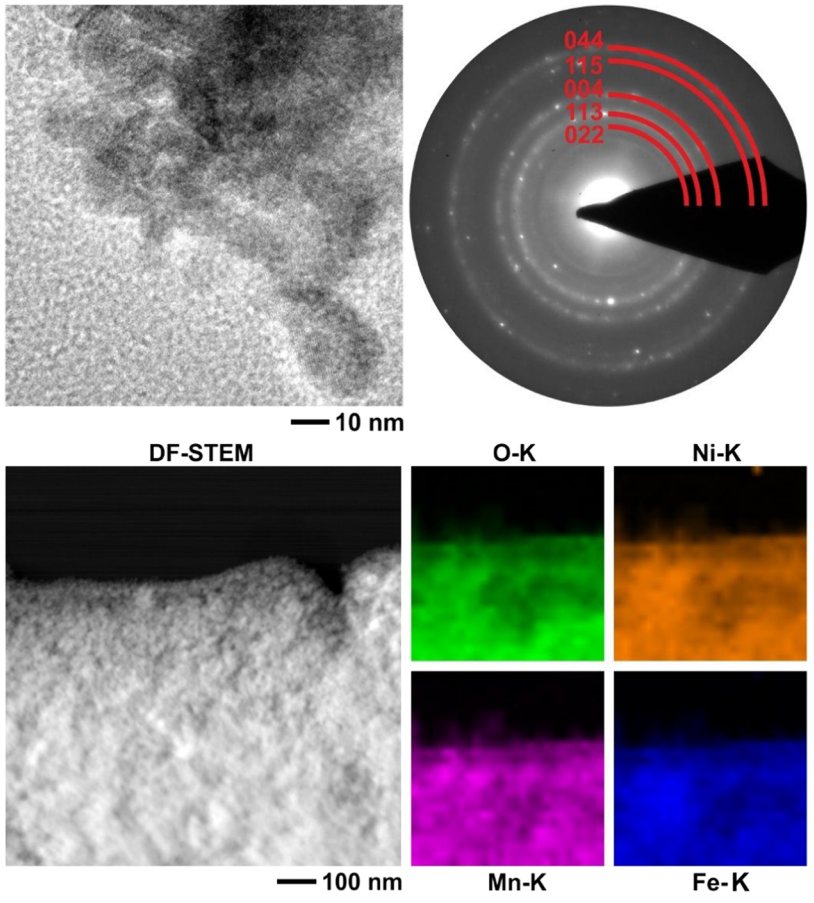

Figure 3. HRTEM micrograph (top left) and SAED pattern (top right) of pristine $NiMnFeO_4$ nanoparticles, STEM-EDX maps at O, Ni, Mn, and Fe K edge in a 0.6 × 1.0 μm^2 area.

$$\mathrm{Fe}_x^{\mathrm{III}}\mathrm{Ni}_y^{\mathrm{II}}\mathrm{Mn}_{3-x-y}^{z}\mathrm{O}_4 \rightarrow a\mathrm{NiO} + \frac{3-a}{3}\mathrm{Fe}_{3/3-a}^{\mathrm{III}}\mathrm{Ni}_{3(1-a)/3-a}^{\mathrm{II}}\mathrm{Mn}_{2a/3-a}^{\mathrm{II}}\mathrm{Mn}_{3-2a/3-a}^{\mathrm{III}}\mathrm{O}_4 + \frac{a}{6}\mathrm{O}_2 \quad (1)$$

Assuming aNiO = 0.48 mol %, the stoichiometry of the spinel should be $Fe^{III}_{1.19}Ni^{II}_{0.61}Mn^{II}_{0.38}Mn^{III}_{0.81}O_4$.

Total scattering experiments allowed an even more accurate understanding of the structure. In Figure 2, the local structure of two models is compared with the resulting PDF. Model I: the cubic spinel, derived by Rietveld refinement; model II: a tetragonally distorted spinel (space group $I4_1/amd$) combined with the presence of cubic NiO. As can be seen in Figure 2, the local PDF is more precisely described by model II. In a

DOI: 10.1021/acsomega.8b03276
ACS Omega 2019, 4, 2398−2409

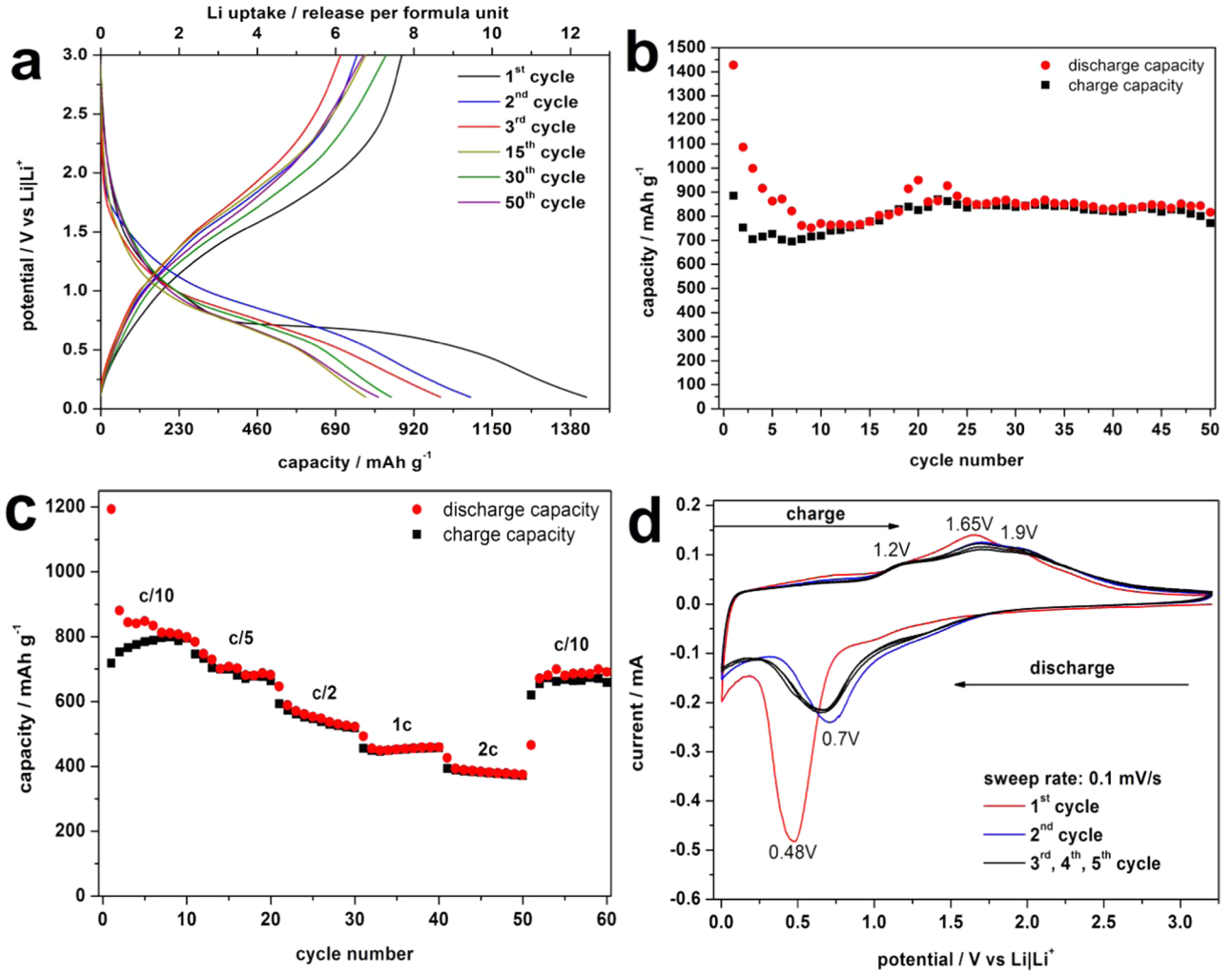

Figure 4. Electrochemical performance of $NiMnFeO_4$ nanoparticles in a potential range from 0.1 to 3 V: (a) potential curves during galvanostatic, 115 mAh/g ≈ 1 Li cycling, (b) capacity of galvanostatic cycling during the first 50 cycles, (c) capacity during cycling at different currents, and (d) cyclic voltammetry (CV) in a potential range from 0 to 3.2 V, with a sweep rate of 0.1 mV/s.

Rietveld-like approach, the lattice parameters of the spinel were determined as a = 5.952(4) Å and c = 8.29(1) Å, with a c/a ratio of 1.392 significantly deviating from the ideal value of 1.4142 = $\sqrt{2}$ expected for cubic symmetry. We note that R_{wp} values for different models do not allow a resolute decision on what model is correct, because these values can be lowered simply by introducing more parameters to the fit. But many features in the PDF are clearly better described using model II and should therefore be a more suitable description of the local structure (Figure 2, right).

As mentioned above, the reduction of cubic symmetry to tetragonal was reported for several manganese-containing spinels[29,33−35] and is a consequence of the Jahn−Teller effect of the Mn^{3+} ions located on tetrahedral and/or octahedral sites. On a tetrahedral site, the degeneracy of the d^4 electronic configuration is removed, leading to a flattening of the MnO_4 tetrahedron whereas for Mn^{3+} on an octahedral site, an elongation of MnO_6 octahedra is expected. We note that $NiMnFeO_4$ adopts cubic symmetry if the sample was prepared at higher temperatures.[36,49,50] Remarkably, a Rietveld refinement of the XRD pattern using the tetragonal model yielded no improvement of the refinement (better R value). This emphasizes that the tetragonal distortion is a local phenomenon and is averaged out into a strained yet still cubic symmetry on a global scale. The results of PDF and Rietveld refinements are compared in Table S1.

As mentioned in the introduction, Larson et al. determined the critical concentration of Mn^{3+} on the octahedral B site to be ∼58−65%.[35] This value is significantly larger than the ≈41% Mn^{3+} assigned to the spinel in this study and may explain why the tetragonal distortion is merely a local phenomenon.

TEM-EDX experiments were performed to verify that the elements are evenly distributed over a large area of the sample. Hence, data were measured at four different positions of the $NiMnFeO_4$ sample, yielding Mn, 35.5 atom %; Fe, 32.4 atom %; and Ni, 32.1 atom % (Supporting Information Table S2), which is close to the desired composition. We note that no region could be found where the composition significantly deviated from the data listed in Table S2.

Agglomerated particles with sizes in the range of 8−12 nm were observed, which represent the number-weighted average and are therefore smaller than the volume-weighted mean obtained by Rietveld refinement of XRD data (Table S1). The HRTEM micrograph (Figure 3, top left) depicts a respective agglomeration of particles that feature a crystalline character, and the corresponding selected area electron diffraction (SAED) pattern (Figure 3, top right) can be assigned to the

DOI: 10.1021/acsomega.8b03276
ACS Omega 2019, 4, 2398−2409

cubic spinel phase (space group $Fd\bar{3}m$, Supporting Information Table S3). Pristine $NiMnFeO_4$ nanoparticles were analyzed by TEM-EDX mapping (Figure 3, bottom) demonstrating a homogeneous dispersion of Ni, Mn, Fe, and O.

2.2. Electrochemical Performance. The electrochemical performance of the $NiMnFeO_4$ nanoparticles was determined with galvanostatic cycling in a potential range from 0.1 to 3.0 V (Figure 4). The capacity for the first discharge amounts to 1427 mAh/g, which is larger than the theoretical value (918 mAh/g). This observation is a common feature for transition-metal oxides and is explained by formation of a solid electrolyte interphase (SEI), formation of a gel-type layer on metal nanoparticles upon deep discharge,[8,51−53] and/or interfacial storage of Li.[54] During the first discharge, the voltage decreases until about 3 Li/fu are consumed. Further Li uptake is accompanied by a flat voltage region at 0.7 V, which is typical for a two-phase reaction. The observation of only one plateau instead of three, which may be expected from different potentials, indicates simultaneous reduction of the cations. After uptake of 9 Li/fu, a sloping region follows up to the discharge limit of 0.1 V. The first charge curve significantly differs from the first discharge curve, which is a typical feature of conversion reactions. The capacity slightly decreases during the first 10 cycles (Figure 4b) and is stable at about 830 mAh/g during the next 40 cycles (Figure 4b).

The reversible capacity for the first cycle of 885 mAh/g (capacity loss 38%) is close to the theoretical value for phase pure $NiMnFeO_4$ of 918 mAh/g. With the phases discussed above, which are slightly oxygen deficient compared with a phase pure spinel (0.48 mol % NiO, 0.84 mol % $Fe^{III}_{1.19}Ni^{II}_{0.61}Mn^{II}_{0.38}Mn^{III}_{0.81}O_4$), the experimental reversible capacity is even closer to the theoretical value of 893 mAh/g. Discharging and charging of the material at different currents (different C rates) is displayed in Figure 4c. For the C/10 rate, the capacity is about 830 mAh/g and an increase of the current leads to lower values: C/5 ≈ 700 mAh/g, C/2 ≈ 550 mAh/g, 1C ≈ 450 mAh/g, and 2C ≈ 380 mAh/g. After fast cycling at 2C, the material is still intact and the capacity reaches ≈700 mAh/g for the cycles 50−60 applying a C/10 rate.

The cyclic voltammetry (CV) curves measured in a potential range from 3.2 to 0 V are presented in Figure 4d. A characteristic feature of conversion-type materials is the pronounced difference between the first and subsequent cycles. In the first discharge curve, a strong anodic signal is observed at about 0.5 V and the first charge curve exhibits not well-resolved weak cathodic signals between about 1.2 and 2.3 V. In the second discharge curve, the anodic event shifted to 0.7 V and shows a clearly reduced intensity. A further slight shift to 0.8 V of this signal is observed in the following discharge curves, whereas the charge curves are characterized by weak and broad signals.

2.3. Operando XAS. The potential curve recorded during the first discharge of the in situ XAS cell is shown in Figure 5, which is similar to that observed in the galvanostatic measurement with Swagelok-type cells (see Section 2.2). The lower capacity is caused by the construction of the cell: for experimental reasons, no spring could be used in the in situ cell and therefore a small part of the material is electrochemically inactive.

The X-ray absorption near-edge spectra (XANES) obtained at the Mn, Fe, and Ni K edges are depicted in Figure 6. For absorber atoms in a centrosymmetric environment, a pre-edge signal is very weak, because the 1s → 3d transition is dipole-forbidden but quadrupole-allowed. In a non-centrosymmetric environment, hybridization of 3d and 4p orbitals is possible, thus adding some p-character to the 3d orbitals. In this situation, a pre-edge feature appears in the XANES spectra. Because pre-edge signals are only observed at the K edges of Mn and Fe, it can be assumed that both Mn^{3+} and Fe^{3+} cations are located on tetrahedral sites. A distribution of Mn^{3+}/Fe^{3+} over the two sites was reported for cubic $NiMnFeO_4$ synthesized at elevated temperatures.[36,49,50] Although the occupation pattern of the sites seems to be obvious, the ratio of Mn^{3+} and Fe^{3+} on the tetrahedral site cannot be determined using the present experimental data. In all three spectra (Figure 6), an intense signal is observed that is due to the spin-allowed 1s → 4p transition. An assignment of oxidation states and/or identification of the chemical composition using XANES is not straightforward for nanosized samples, as discussed, e.g., in refs 55, 56. In addition, evaluation of the oxidation state is not accurate because edge shifts may also arise from structural distortions and defects.

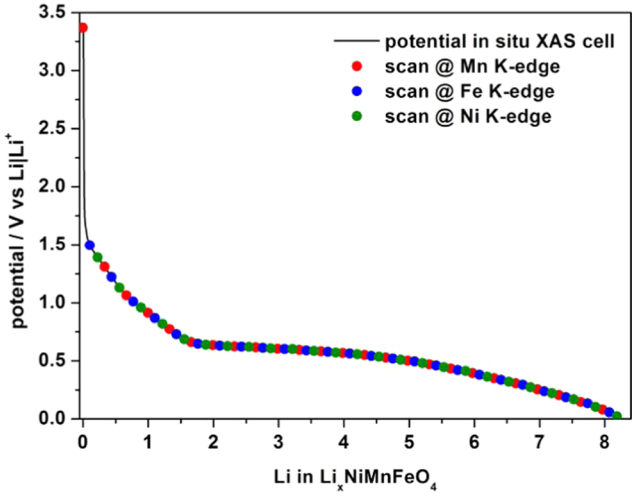

Figure 5. Potential curve of the in situ XAS cell.

At the early stages of Li uptake up to ≈0.8 Li/fu, the spectra are not affected (blue lines in the spectra in Figure 6). Increasing continuously, the Li content leads to a shift of the Fe and Mn K edge energies and of the signal of the 1s → 4p transition to lower energies, indicating successive reduction of Fe^{3+}/Mn^{3+} to Fe^{2+}/Mn^{2+} (Figure 6, top left and top right). The disappearance of the pre-edge feature in the spectra of Mn and Fe is a hint that the reduced cations moved from the tetrahedral sites to empty octahedra. Up to about 3 Li/fu, the Ni K edge is not significantly affected and a similar observation was made for $NiFe_2O_4$[68] and $NiCo_2O_4$,[69] where only minor changes of the spectral signature of the Ni K edge could be identified.

Li uptake by the host material beyond 3 Li/fu leads to a successive reduction of the intensity of the 1s → 4p signal and a further shift of the edge energies to lower values, indicating reduction of the transition-metal cations. Furthermore, a pre-edge feature occurs in all spectra, which is typical for the metallic state. A rotation around isosbestic points occurs, which are located at 6545 eV for Mn, 7123 eV for Fe, and 8341 eV for Ni, suggesting no intermediate reaction steps during reduction of the cations.

2.4. Operando XRD. Operando XRD investigations enable observations of structural changes on the long-range order and

DOI: 10.1021/acsomega.8b03276
ACS Omega 2019, 4, 2398−2409

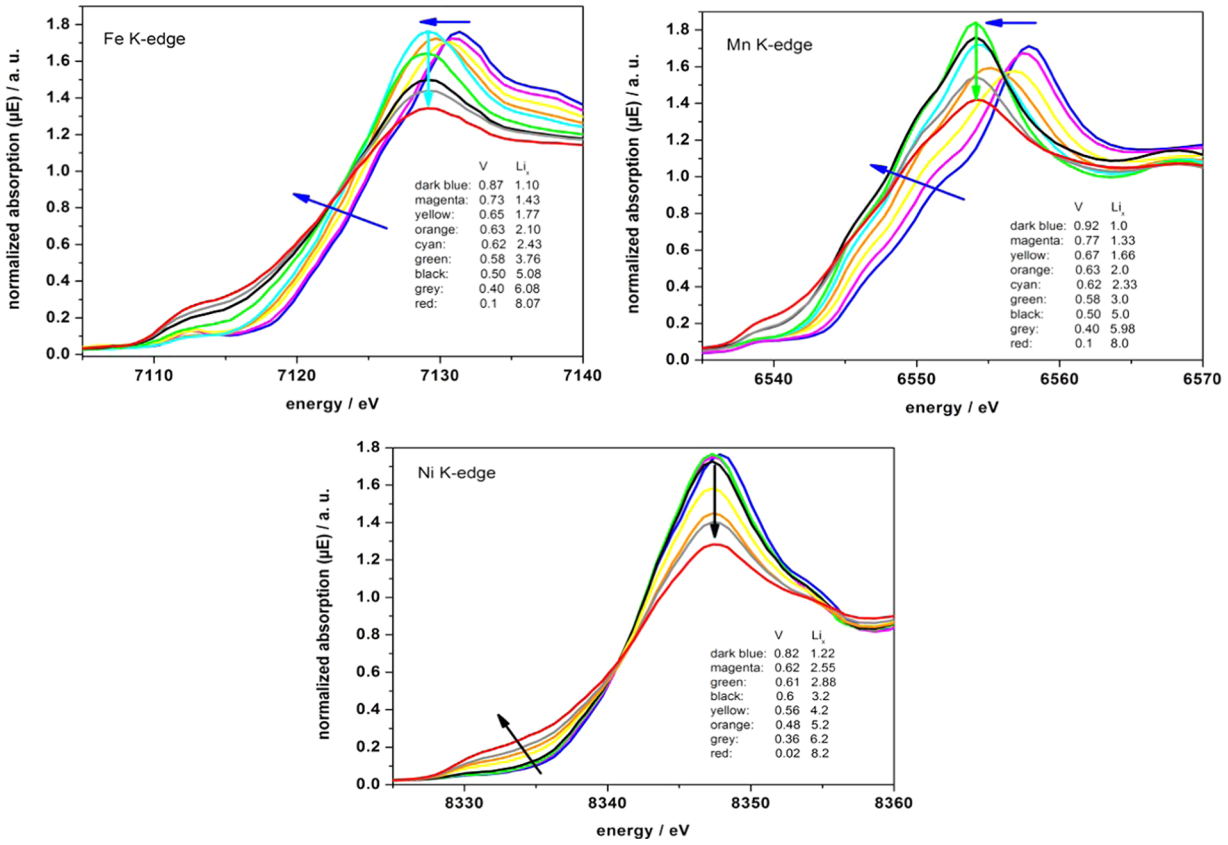

Figure 6. Operando XAS spectra at Fe K edge (top, left), Mn K edge (top, right), and Ni K edge (bottom) collected during the first discharge process. In the insets, the color codes are explained reporting the voltage (V) and the Li content (Li_x) according to the discharge profile shown in Figure 5.

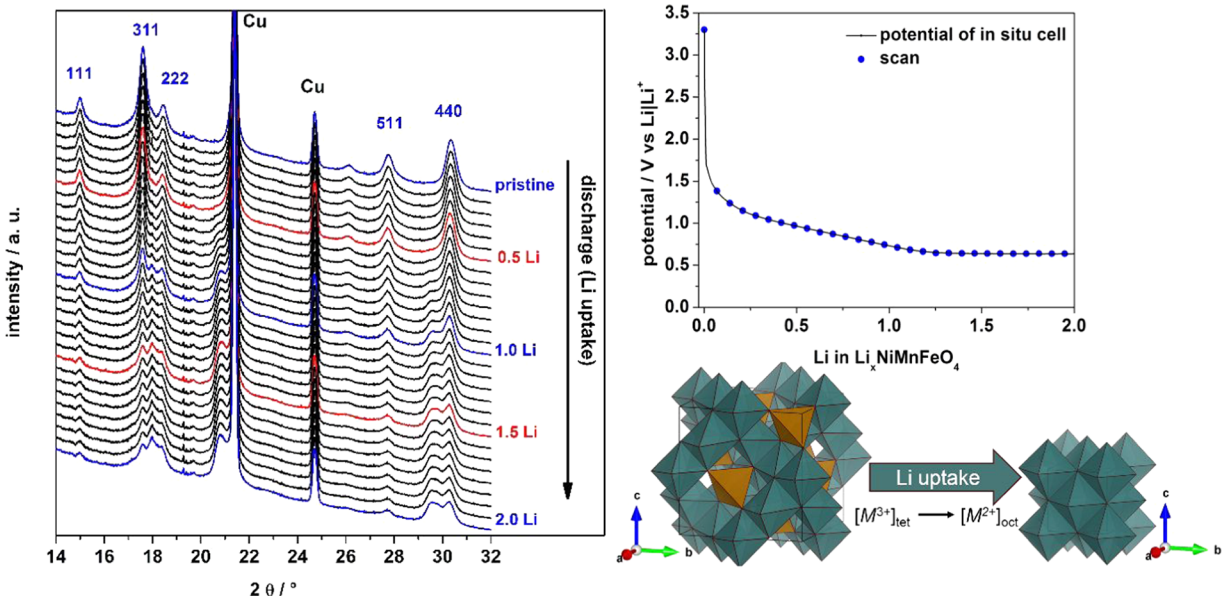

Figure 7. Operando XRD powder pattern during uptake of the first 2 Li/fu (left). The two reflections of metallic Cu are caused by the cell setup. Potential of the in situ cell (upper right). Schematic picture of structural changes during Li uptake (lower right).

formation of new crystalline phases. Figure 7 shows the XRD patterns recorded during uptake of 2 Li/fu.

During uptake of the first 0.5 Li/fu, the position of the reflections is not affected (Figure 7) and first indications of structural changes can be observed as shoulders on the lower scattering angle side of the reflections for ≈0.7−0.8 Li/fu. This observation is in accordance with the results of XANES experiments discussed in the previous section. The shoulders in the XRD patterns clearly develop into Bragg reflections with increasing Li content, and at 2 Li/fu, it seems that two phases coexist. In principle, the reflections of elemental Cu can be used as an internal standard for Rietveld refinements of the

DOI: 10.1021/acsomega.8b03276
ACS Omega 2019, 4, 2398−2409

powder patterns. But a buckling of the cell caused deviations of the relative peak positions from their theoretical values, thus preventing reliable refinements of the operando data. Therefore, additional ex situ XRD and PDF measurements of a sample after uptake of 2 Li/fu were collected to elucidate the structural behavior. The XRD pattern reveals the existence of two rock salt monoxide phases, NiO (a = 4.1872(2) Å) and another rock salt monoxide, whose lattice parameter indicates the presumably mixed monoxide (NiMnFe)O with a = 4.2809(3) Å (for comparison: FeO ICSD 27854 a = 4.308 Å; MnO ICSD 18006 a = 4.480 Å; NiO ICSD 28834 a = 4.170 Å), but the spinel phase is also present (Figures 7 and S1). Nevertheless, the PDF demonstrates that all major features of the local region can be sufficiently well described by a model consisting of the above-mentioned mixed monoxide and NiO only (Figure 8 and Table S4).

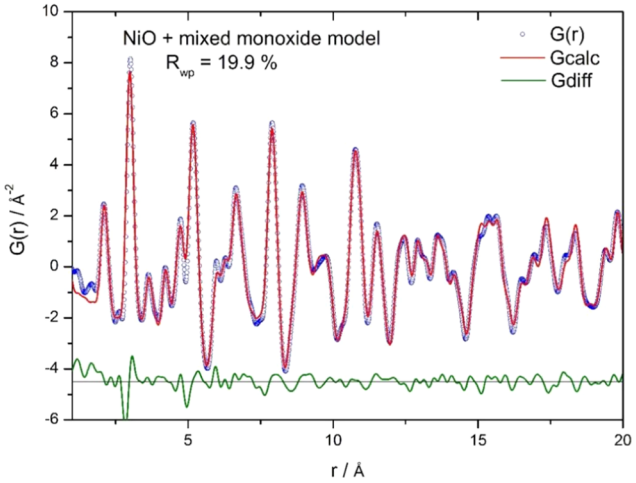

Figure 8. PDF of a sample after uptake of 2 Li/fu obtained from total scattering experiments at beamline P02.1, DESY. A model comprising NiO and a mixed (NiFeMn)O was used to calculate the PDF (red). The R_{wp} value was determined in a Rietveld-like least squares refinement and is sufficiently low for PDF measurements, indicating a suitable description of the local structure.

A closer look on the modeled PDF shows that some minor deviations are still present (Figure 8), suggesting that the model still exhibits some inaccuracies. Initially, several defect monoxide phases, like Ni_6MnO_8, were tested but no improvement of the fit could be achieved. Therefore, the difference function (green curve in Figure 8) was compared to modeled PDFs of common Li compounds described in the literature (Figures 9 and S2), e.g., refs 7, 57, 58. Although often discussed as the major Li compounds generated during SEI formation, only minor agreements with Li_2O, LiF, or Li_2CO_3 can be observed (Figure S2) but reasonably good matches are obtained using LiOH in the further phase.

The occurrence of LiOH was reported in the literature, which is generated by reaction between Li and an OH layer being naturally present on nanoscopic metal oxide particles, which, e.g., were detected on Fe_3O_4 nanoparticles.[58,59]

We also compared the PDF of the pristine material with that measured after uptake of 2 Li/fu (Figure S2). Pronounced differences in positions and intensities can be seen, which are caused by changes of the distribution of transition-metal cations over the tetrahedral and octahedral sites: distances related to tetrahedral sites clearly decreased and those related

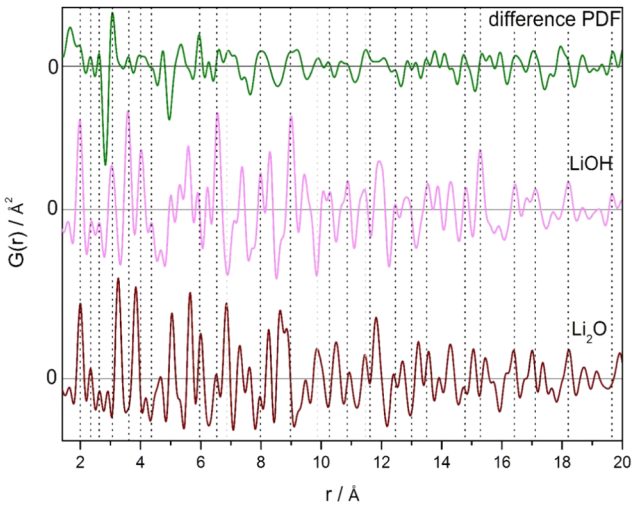

Figure 9. Comparison of difference PDF from Figure 8 with modeled PDFs of LiOH and Li_2O. Coinciding distances of LiOH are marked by a black dashed line, and those of Li_2O, in light gray.

to octahedral sites are more intense. This finding implies the movement of the majority of cations from tetrahedral to octahedral sites.

Beyond 2 Li/fu, a continuous decrease and broadening of the reflections can be observed. At the end of discharge, all reflections disappeared (Figure 10), suggesting formation of amorphous materials or of particles being too small to be detected by X-rays.

For nanosized spinel oxides, we also observed that at the early stages of Li uptake, first an amorphous layer is consumed and depending on the material significant changes in the XRD patterns, occurring only for $Li_xM_2O_4$ with $x \geq 0.3-0.5$. A similar observation was reported for Li uptake by Mn_3O_4.[60]

2.5. Ex Situ XAS. Additional ex situ XAS spectra were collected after 1, 2, 3, and 5 cycles (Figure 11) because operando XAS only probed the first cycle. The spectra of the pristine material are similar for all three K edges, as observed in the operando experiment (Figure 11, blue line). At the end of the first discharge process, Mn^{3+}, Fe^{3+}, and Ni^{2+} are reduced and a comparison with the spectra of the metal references reveals that the cations are reduced to the metallic state (Figure 11, black straight and dashed line). The differences between the spectra of the metallic foils and those of the reduced metallic nanoparticles may be caused by the large number of atoms on the surface of the nanoparticles, the very small particle sizes, and a high density of defects. In addition, the nanoparticles are embedded in an oxygen-containing matrix and the surface of the particles may be partially oxidized, an example of these effects was reported in ref 61. After the first cycle, the Mn K-edge energy exhibits a clear shift to lower energy, indicating that the oxidation state observed for the pristine material is not reached (Figure 11, top left), which may partially explain the capacity loss during cycling.

In the following cycles, the Mn K-edge energy is not significantly altered but changes are observed for the 1s → 4p transition, which may be caused by distortions and defects in the nanosized particles.

The energy of the Fe K edge shows no pronounced differences between the 1st and 5th cycle (Figure 11, top right), and is similar to that of the pristine material. This observation indicates that reduction and oxidation of Fe^0 ↔

DOI: 10.1021/acsomega.8b03276
ACS Omega 2019, 4, 2398−2409

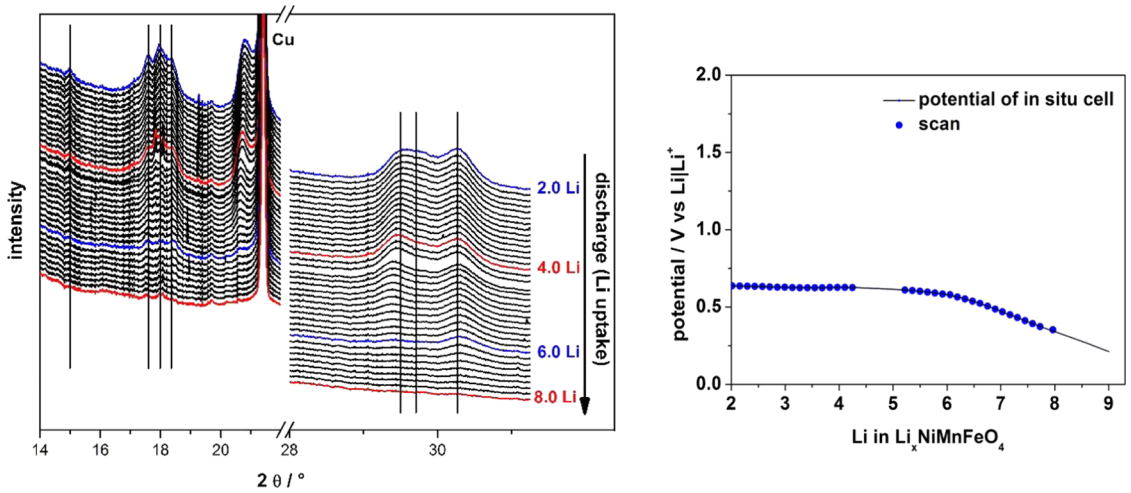

Figure 10. In situ powder diffraction pattern during uptake of more than 2 Li/fu (left) and potential of the in situ cell during operation (right).

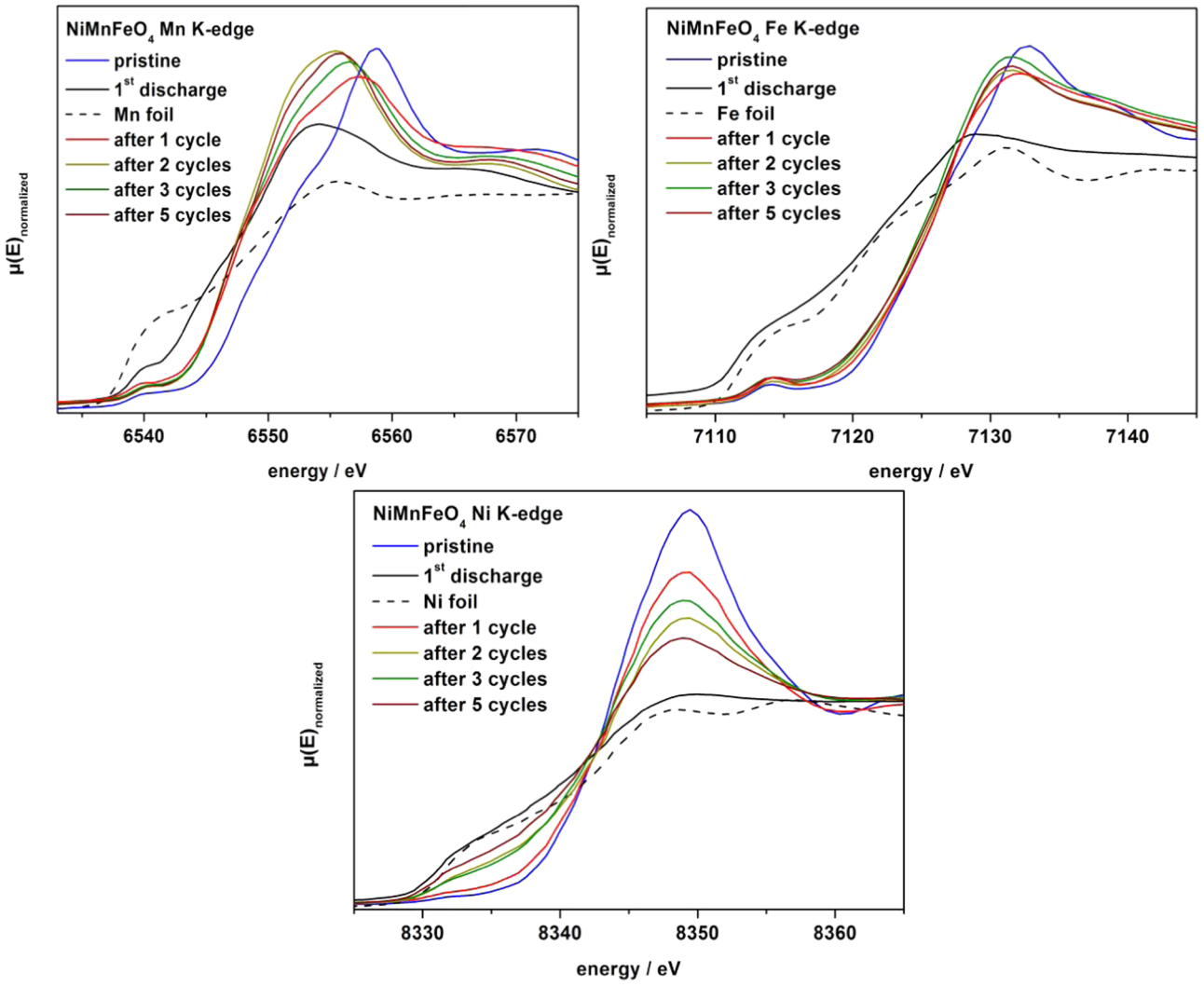

Figure 11. Ex situ XAS spectra at Mn K edge (top, left), Fe K edge (top, right), and Ni K edge (bottom) of pristine $NiMnFeO_4$ (blue), after the first discharge (black straight line) and after 1 (red), 2 (yellow), 3 (green), and 5 cycles (dark red).

Fe^{3+} is reversible over many cycles. In contrast, the Ni K edge (Figure 11, bottom) exhibits a significant reduction of the 1s → 4p transition and the shape of the signal becomes more and more similar to that of the metallic reference foil with increasing number of cycles. These findings indicate that the $Ni^0 \leftrightarrow Ni^{2+}$ redox reaction is not stable over many cycles and a part of Ni remains in the metallic state. This is maybe another reason for the capacity loss during cycling (see Section 2.2).

DOI: 10.1021/acsomega.8b03276
ACS Omega 2019, 4, 2398−2409

2.6. Ex Situ ^{7}Li MAS NMR. XAS data yields information only about the transition metals, but no information about the direct environment of the lithium ions is available. ^{7}Li MAS NMR closes this gap of information. Paramagnetic ions in the direct neighborhood of Li^+ ions can have strong effects on the NMR spectra, leading to large shift values.[62] ^{7}Li MAS NMR spectra of $NiMnFeO_4$ nanoparticles after uptake of 2 Li/fu and after complete discharge are displayed in Figure 12. The

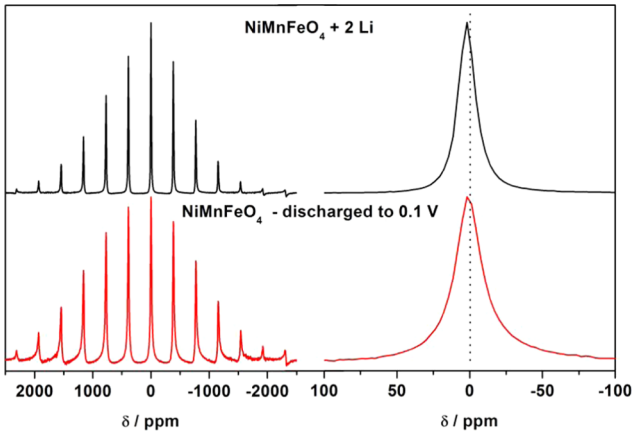

Figure 12. ^{7}Li MAS NMR spectra of $NiMnFeO_4$ nanoparticles after insertion of 2 Li (black) and after discharge to 0.1 V (red). Left: full spinning sideband patterns; right: magnified view of the region of the isotropic peaks.

spectrum measured after uptake of 2 Li/fu shows a narrow isotropic peak close to 0 ppm (Figure 12, black) and narrow spinning sidebands. Hence, paramagnetic neighbors in the direct environment of Li can be excluded due to the small shift.[57,63] This indicates formation of a Li-containing phase without transition metals. The NMR spectrum acquired after discharge to 0.1 V shows a similar shift close to 0 ppm. Obviously, the only Li-containing phase must exhibit a diamagnetic environment, e.g., LiOH, Li_2O, or Li_2CO_3. But the isotropic peaks are broadened and the width of the spinning sideband pattern is increased (Figure 12, red line). This behavior is caused by the formation and growth of metallic Ni, Mn, and Fe particles. Similar observations were made in prior studies for $MnFe_2O_4$ and $MgFe_2O_4$.[37,38]

3. CONCLUSIONS

The true compositional and structural nature of nanoparticles of the intended spinel $NiMnFeO_4$ could only be determined applying advanced X-ray scattering techniques. According to the results of X-ray diffraction and PDF analyses, $NiMnFeO_4$ consists of a mixture of a strained spinel and NiO, both being present as intergrown nanoparticles. The estimated stoichiometry of the spinel is $Fe^{III}_{1.19}Ni^{II}_{0.61}Mn^{II}_{0.38}Mn^{III}_{0.81}O_4$. The sample shows a high specific capacity of >800 mAh/g as Li anode material during 50 cycles. Operando XAS and XRD experiments demonstrate that first Li is consumed without significant structural and electronic changes. Increasing the Li/fu leads to reduction of Fe^{3+}/Mn^{3+} to Fe^{2+}/Mn^{2+} and the simultaneous movement of these cations from tetrahedral sites to empty octahedral sites. This assumption is clearly supported by comparison of the PDFs of the pristine material and a sample containing 2 Li/fu: the signals related to transition-metal cations on tetrahedral sites are significantly reduced, whereas those for cations residing on octahedral sites are increased. The detailed analysis of the PDF of the sample containing 2 Li gives hints that LiOH is formed during Li uptake. This is further supported by ^{7}Li NMR investigations showing a Li signal typical for a diamagnetic environment. The analysis of the total scattering data of the sample with 2 Li/fu presents evidences for the existence of two monoxides, i.e., NiO and (NiMnFe)O crystallizing in a NaCl-like structure. Further increase of the Li content leads to a successive conversion of the cations to the metallic state, and the nanoparticles/amorphous particles are embedded in a Li-containing matrix. The capacity loss observed during the first few cycles can be at least partially traced back to the inability to reoxidize metallic Mn to Mn^{3+} and successively occurring inactivity of Ni nanoparticles.

4. EXPERIMENTAL SECTION

4.1. Synthesis. $NiFeMnO_4$ nanoparticles were synthesized by dissolving 5 mmol $Ni(NO_3)_2{\cdot}6H_2O$ (97%, Merck), 5 mmol $Fe(NO_3)_3{\cdot}9H_2O$ (98%, Riedel-de Haen), and 5 mmol $Mn(NO_3)_2{\cdot}4H_2O$ (98%, Grüssing) in 20 mL of deionized water. Five milliliters of nitric acid (65%, p.A., Grüssing) were added to the solution by stirring at room temperature. Afterward, 10 mL of ethylene glycol (99%, Merck Millipore) were added and the mixture was heated at 80 °C until a viscous gel is formed. Afterward, the gel was dried at 120 °C for 24 h. The solid was ground in an agate mortar and calcined at 400 °C in a preheated oven in air for 3 h.[43]

4.2. Materials Characterizations. Ex situ XRD and total scattering patterns were collected at beamline P02.1, Petra III, DESY, Hamburg, at a wavelength λ = 0.207 Å (60 keV) and a sample detector distance of 1100 and 385 mm, respectively. The data were collected using a PerkinElmer XRD1621 two-dimensional (2D) detector. The 2D data were processed using DAWN Science.[64] Total scattering data were processed using xPDFsuite to obtain the pair distribution function (Q_{max} 21.66 $Å^{-1}$, Q_{damp} = 0.0215) and PDFgui for modeling and fitting the PDF.[65−67] In both setups, NIST 660a LaB_6 reference material was measured to account for instrumental contributions to XRD and PDF, respectively. To account for the contribution of the glass, an empty capillary was measured and subtracted from the scattering data before PDF calculation. The refinement of the XRD powder patterns was done using Topas Academic 6.0.[47]

Energy-dispersive X-ray spectra were measured in a Philips ESEM XL-30 with EDAX New XL-30 Detecting Unit. Transmission electron microscopy investigations were performed in a Tecnai F30 G2-STwin microscope at 300 kV with a field emission gun cathode and a Si/Li detector (Thermo Fisher, NSS). $NiFeMnO_4$ nanoparticles were suspended in *n*-butanol and treated in an ultrasonic bath to induce particle separation. Afterward, the dispersion was dropped onto a holey-carbon copper grid.

4.3. Electrochemical Measurements. Electrochemical tests were performed in Swagelok cells. The test cells were prepared by mixing 70 wt % active material with 20 wt % SUPER C65 Carbon (Timcal, Switzerland) and 10 wt % sodium polyacrylate (Sigma-Aldrich, Germany). The mixture was dissolved with deionized water, deposited on dendritic copper foil (Schlenk, Germany), and dried at room temperature for 2 days. Afterward, 10 mm disks were cut with about 1 mg of active material per cm^2. Lithium metal (99.9%, abcr Germany) was used as a counter electrode, glass microfiber filters (Whatman, United Kingdom) as the separator, and a solution of 1 M $LiPF_6$ in an ethylene carbonate/dimethyl

DOI: 10.1021/acsomega.8b03276
ACS Omega 2019, 4, 2398−2409

carbonate mixture (BASF, Germany) as electrolyte. The cells were assembled in an argon-filled glovebox (<1 ppm O_2, <1 ppm H_2O). Galvanostatic experiments were performed with MTI BST8-WA, and cyclic voltammetry was measured with a Zahner XPot. A C/10 rate corresponds to the uptake/release of 8 Li/fu within 10 h, which is equal to 91.8 mA/g.

4.4. Operando XRD and XAS. For operando XRD and XAS investigations, a custom-built cell (40 × 40 × 15 mm^3) consisting of two aluminum plates with rectangular apertures (14 × 3 mm^2) in the center and two sheets of Kapton foil windows glued on both sides was used. For these investigations, 80 wt % active material was mixed with 10 wt % SUPER C65 Carbon and 10 wt % poly(vinylidene difluoride) (Solvay, Germany). The mixture was suspended in *N*-methyl-2-pyrrolidinone (99.5%, Sigma-Aldrich) and was deposited on a thin Cu foil, followed by drying in inert atmosphere. The counter electrode Li metal was attached on a perforated Cu foil. As separator, a microporous polyethylene/polypropylene membrane (Celgard) was used and the electrolyte consisted of 1 M $LiPF_6$ in an ethylene carbonate/dimethyl carbonate mixture.

Operando XAS experiments were performed at the XAS beamline at ANKA (Karlsruhe, Germany). The cell was discharged with a C/12 rate during repeated quick XAS scans at the Mn, Fe, and Ni K absorption edges. The time for scanning each absorption edge was 5 min. Energy calibration was done with a Fe foil before and after the experiment. Mn, Fe, and Ni reference foils were measured between the second and third ionization chambers. The spectra were treated in the usual way using Athena Software package.[68]

Operando XRD investigations were performed at the PDIFF beamline at ANKA (Karlsruhe, Germany, 16 keV, λ = 0.774901 Å) with a Princeton CCD detector. The powder patterns were collected within 5 min, and the 2D patterns were transformed with the area diffraction machine.[69]

The Bragg reflection profile of the instrument was determined using LaB_6 standard material (NIST 660a) applying identical conditions. The cells were discharged/charged using a Biologic VSP 300 potentiostat/galvanostat.

4.5. Ex Situ XAS, TEM and ^{7}Li MAS NMR of Lithiated Samples. For ex situ XAS, samples were discharged in Swagelok-type test cells. The lithiated electrodes were removed and glued between adhesive Kapton tape under argon atmosphere. Afterward, samples were inserted into the in situ cells and transferred to the beamline.

TEM measurements were performed with a Tecnai F30 G^2-STwin microscope with a field emission gun cathode operated at 300 kV and a Si/Li detector (Thermo Fisher, NSS). For TEM preparation, $NiFeMnO_4$ particles were suspended in *n*-butanol and dropped on a holey-carbon copper grid.

The ^{7}Li MAS NMR experiments were performed with a 2.5 mm probe on an Avance 200 MHz spectrometer using a magnetic field of 4.7 T. The spectra were collected at an operating frequency of 77.8 MHz. A spinning frequency of 30 kHz and a rotor-synchronized spin-echo sequence (90°−τ−180°−τ-acq.) were used to acquire the spectra. $\pi/2$ pulses of 1 μs were used, with recycle delay times of 1 s. All NMR spectra were referenced to a 1 M LiCl solution, at 0 ppm.

■ ASSOCIATED CONTENT

Supporting Information

The Supporting Information is available free of charge on the ACS Publications website at DOI: 10.1021/acsomega.8b03276.

Rietveld and PDF refinements, EDX data, *d*(*hkl*) data of the SAED pattern, and XRD pattern after uptake of 2 Li/fu (PDF)

■ AUTHOR INFORMATION

Corresponding Author

*E-mail: wbensch@ac.uni-kiel.de. Phone: +494318802091. Fax: +494318801520.

ORCID

Sylvio Indris: 0000-0002-5100-113X

Wolfgang Bensch: 0000-0002-3111-580X

Present Address

⊥Custom Cells Itzehoe GmbH, Fraunhoferstraße 1B, 25524 Itzehoe, Germany (S.P.).

Notes

The authors declare no competing financial interest.

■ ACKNOWLEDGMENTS

We are grateful to the Deutsche Forschungsgemeinschaft and to the German Federal Ministry of Education and Research for financial support. Beamtime allocation by ANKA (Karlsruhe) and DESY (Hamburg) is thankfully acknowledged.

■ REFERENCES

(1) Armand, M.; Tarascon, J.-M. Building Better Batteries. *Nature* **2008**, *451*, 652−657.

(2) Etacheri, V.; Marom, R.; Elazari, R.; Salitra, G.; Aurbach, D. Challenges in the Development of Advanced Li-Ion Batteries: A Review. *Energy Environ. Sci.* **2011**, *4*, 3243−3262.

(3) Scrosati, B. Challenge of Portable Power. *Nature* **1995**, *373*, 557−558.

(4) Tarascon, J.-M.; Armand, M. Issues and Challenges Facing Rechargeable Lithium Batteries. *Nature* **2001**, *414*, 359−367.

(5) Choi, N.-S.; Chen, Z.; Freunberger, S. A.; Ji, X.; Sun, Y.-K.; Amine, K.; Yushin, G.; Nazar, L. F.; Cho, J.; Bruce, P. G. Lithiumbatterien und elektrische Doppelschichtkondensatoren: aktuelle Herausforderungen. *Angew. Chem.* **2012**, *124*, 10134−10166.

(6) Palacín, M. R. Understanding Ageing in Li-Ion Batteries: A Chemical Issue. *Chem. Soc. Rev.* **2018**, *47*, 4924−4933.

(7) Xu, K. Electrolytes and Interphases in Li-Ion Batteries and Beyond. *Chem. Rev.* **2014**, *114*, 11503−11618.

(8) Poizot, P.; Laruelle, S.; Grugeon, S.; Dupont, L.; Tarascon, J.-M. Nano-Sized Transition-Metal Oxides as Negative-Electrode Materials for Lithium-Ion Batteries. *Nature* **2000**, *407*, 496−499.

(9) Reddy, M. V.; Subba Rao, G. V.; Chowdari, B. V. R. Metal Oxides and Oxysalts as Anode Materials for Li Ion Batteries. *Chem. Rev.* **2013**, *113*, 5364−5457.

(10) Wang, Y.; Wang, M.; Chen, G.; Dong, C.; Wang, Y.; Fan, L.-Z. Surfactant-Mediated Synthesis of $ZnCo_2O_4$ Powders as a High-Performance Anode Material for Li-Ion Batteries. *Ionics* **2015**, *21*, 623−628.

(11) Wu, X.; Li, S.; Wang, B.; Liu, J.; Yu, M. Controllable Synthesis of Micro/Nano-Structured $MnCo_2O_4$ with Multiporous Core−Shell Architectures as High-Performance Anode Materials for Lithium-Ion Batteries. *New J. Chem.* **2015**, *39*, 8416−8423.

(12) Zhang, W.; Hou, X.; Lin, Z.; Yao, L.; Wang, X.; Gao, Y.; Hu, S. Hollow Microspheres and Nanoparticles $MnFe_2O_4$ as Superior Anode Materials for Lithium Ion Batteries. *J. Mater. Sci.: Mater. Electron.* **2015**, *26*, 9535−9545.

DOI: 10.1021/acsomega.8b03276
ACS Omega 2019, 4, 2398−2409

(13) Fontcuberta, J.; Rodríguez, J.; Pernet, M.; Longworth, G.; Goodenough, J. B. Structural and Magnetic Characterization of the Lithiated Iron Oxide $Li_xFe_3O_4$. *J. Appl. Phys.* **1986**, *59*, 1918−1926.
(14) Thackeray, M. M.; David, W. I. F.; Goodenough, J. B. Structural Characterization of the Lithiated Iron Oxides $Li_xFe_3O_4$ and $Li_xFe_2O_3$ ($0 < x < 2$). *Mater. Res. Bull.* **1982**, *17*, 785−793.
(15) Larcher, D.; Sudant, G.; Leriche, J.-B.; Chabre, Y.; Tarascon, J.-M. The Electrochemical Reduction of Co_3O_4 in a Lithium Cell. *J. Electrochem. Soc.* **2002**, *149*, A234−A241.
(16) Li, Y.; Tan, B.; Wu, Y. Mesoporous Co_3O_4 Nanowire Arrays for Lithium Ion Batteries with High Capacity and Rate Capability. *Nano Lett.* **2008**, *8*, 265−270.
(17) Binotto, G.; Larcher, D.; Prakash, A. S.; Herrera Urbina, R.; Hegde, M. S.; Tarascon, J.-M. Synthesis, Characterization, and Li-Electrochemical Performance of Highly Porous Co_3O_4 Powders. *Chem. Mater.* **2007**, *19*, 3032−3040.
(18) Lavela, P.; Tirado, J. L. $CoFe_2O_4$ and $NiFe_2O_4$ Synthesized by Sol−Gel Procedures for Their Use as Anode Materials for Li Ion Batteries. *J. Power Sources* **2007**, *172*, 379−387.
(19) Cabana, J.; Monconduit, L.; Larcher, D.; Palacín, M. R. Beyond Intercalation-Based Li-Ion Batteries: The State of the Art and Challenges of Electrode Materials Reacting Through Conversion Reactions. *Adv. Mater.* **2010**, *22*, E170−E192.
(20) Courtel, F. M.; Duncan, H.; Abu-Lebdeh, Y.; Davidson, I. J. High Capacity Anode Materials for Li-Ion Batteries Based on Spinel Metal Oxides AMn_2O_4 (A = Co, Ni, and Zn). *J. Mater. Chem.* **2011**, *21*, 10206−10218.
(21) Bruce, P. G.; Scrosati, B.; Tarascon, J.-M. Nanomaterials for Rechargeable Lithium Batteries. *Angew. Chem., Int. Ed.* **2008**, *47*, 2930−2946.
(22) Nazar, L. F.; Goward, G.; Leroux, F.; Duncan, M.; Huang, H.; Kerr, T.; Gaubicher, J. Nanostructured Materials for Energy Storage. *Int. J. Inorg. Mater.* **2001**, *3*, 191−200.
(23) Arico, A. S.; Bruce, P.; Scrosati, B.; Tarascon, J.-M.; Van Schalkwijk, W. *Materials for Sustainable Energy*; Co-Published with Macmillan Publishers Ltd: UK, 2010; pp 148−159.
(24) Zhao, H.; Zheng, Z.; Wong, K. W.; Wang, S.; Huang, B.; Li, D. Fabrication and Electrochemical Performance of Nickel Ferrite Nanoparticles as Anode Material in Lithium Ion Batteries. *Electrochem. Commun.* **2007**, *9*, 2606−2610.
(25) Kang, W.; Tang, Y.; Li, W.; Yang, X.; Xue, H.; Yang, Q.; Lee, C.-S. High Interfacial Storage Capability of Porous $NiMn_2O_4$ /C Hierarchical Tremella-like Nanostructures as the Lithium Ion Battery Anode. *Nanoscale* **2015**, *7*, 225−231.
(26) Cherian, C. T.; Reddy, M. V.; Rao, G. V. S.; Sow, C. H.; Chowdari, B. V. R. Li-Cycling Properties of Nano-Crystalline $(Ni_{1-x}Zn_x)Fe_2O_4$ ($0 \le x \le 1$). *J. Solid State Electrochem.* **2012**, *16*, 1823−1832.
(27) NuLi, Y.-N.; Qin, Q.-Z. Nanocrystalline Transition Metal Ferrite Thin Films Prepared by an Electrochemical Route for Li-Ion Batteries. *J. Power Sources* **2005**, *142*, 292−297.
(28) Fu, Y.; Wan, Y.; Xia, H.; Wang, X. Nickel Ferrite−Graphene Heteroarchitectures: Toward High-Performance Anode Materials for Lithium-Ion Batteries. *J. Power Sources* **2012**, *213*, 338−342.
(29) Ma, Y.; Tai, C.-W.; Younesi, R.; Gustafsson, T.; Lee, J. Y.; Edström, K. Iron Doping in Spinel $NiMn_2O_4$: Stabilization of the Mesoporous Cubic Phase and Kinetics Activation toward Highly Reversible Li+ Storage. *Chem. Mater.* **2015**, *27*, 7698−7709.
(30) Zhao, H.; Liu, L.; Hu, Z.; Sun, L.; Han, S.; Liu, Y.; Chen, D.; Liu, X. Neutron Diffraction Analysis and Electrochemical Performance of Spinel $Ni(Mn_{2-x}Co_x)O_4$ as Anode Materials for Lithium Ion Battery. *Mater. Res. Bull.* **2016**, *77*, 265−270.
(31) Feltz, A.; Pölzl, W. Spinel Forming Ceramics of the System $Fe_xNi_yMn_{3-x-y}O_4$ for High Temperature NTC Thermistor Applications. *J. Eur. Ceram. Soc.* **2000**, *20*, 2353−2366.
(32) Macklen, E. D. Electrical Conductivity and Cation Distribution in Nickel Manganite. *J. Phys. Chem. Solids* **1986**, *47*, 1073−1079.
(33) Darul, J.; Lathe, C.; Piszora, P. Hooked on Switch: Strain-Managed Cooperative Jahn−Teller Effect in $Li_{0.95}Mn_{2.05}O_4$ Spinel. *RSC Adv.* **2014**, *4*, 65205−65212.
(34) Bodak, O.; Akselrud, L.; Demchenko, P.; Kotur, B.; Mrooz, O.; Hadzaman, I.; Shpotyuk, O.; Aldinger, F.; Seifert, H.; Volkov, S.; Pekhnyo, V. Microstructure, Crystal Structure and Electrical Properties of $Cu_{0.1}Ni_{0.8}Co_{0.2}Mn_{1.9}O_4$ Ceramics Obtained at Different Sintering Conditions. *J. Alloys Compd.* **2002**, *347*, 14−23.
(35) Larson, E. G.; Arnott, R. J.; Wickham, D. G. Preparation, Semiconduction and Low-Temperature Magnetization of the System $Ni_{1-x}Mn_{2+x}O_4$. *J. Phys. Chem. Solids* **1962**, *23*, 1771−1781.
(36) Lavela, P.; Kyerematen, N. A.; Tirado, J. L. $NiMn_{2-x}Fe_xO_4$ Prepared by a Reverse Micelles Method as Conversion Anode Materials for Li-Ion Batteries. *Mater. Chem. Phys.* **2010**, *124*, 102−108.
(37) Permien, S.; Hain, H.; Scheuermann, M.; Mangold, S.; Mereacre, V.; Powell, A. K.; Indris, S.; Schürmann, U.; Kienle, L.; Duppel, V.; Harm, S.; Bensch, W. Electrochemical Insertion of Li into Nanocrystalline $MnFe_2O_4$: A Study of the Reaction Mechanism. *RSC Adv.* **2013**, *3*, 23001.
(38) Permien, S.; Indris, S.; Scheuermann, M.; Schürmann, U.; Mereacre, V.; Powell, A. K.; Kienle, L.; Bensch, W. Is There a Universal Reaction Mechanism of Li Insertion into Oxidic Spinels: A Case Study Using $MgFe_2O_4$. *J. Mater. Chem. A* **2015**, *3*, 1549−1561.
(39) Permien, S.; Indris, S.; Schürmann, U.; Kienle, L.; Zander, S.; Doyle, S.; Bensch, W. What Happens Structurally and Electronically during the Li Conversion Reaction of $CoFe_2O_4$ Nanoparticles: An Operando XAS and XRD Investigation. *Chem. Mater.* **2016**, *28*, 434−444.
(40) Permien, S.; Indris, S.; Hansen, A.-L.; Scheuermann, M.; Zahn, D.; Schürmann, U.; Neubüser, G.; Kienle, L.; Yegudin, E.; Bensch, W. Elucidation of the Conversion Reaction of $CoMnFeO_4$ Nanoparticles in Lithium Ion Battery Anode via Operando Studies. *ACS Appl. Mater. Interfaces* **2016**, *8*, 15320−15332.
(41) Permien, S.; Indris, S.; Neubüser, G.; Fiedler, A.; Kienle, L.; Zander, S.; Doyle, S.; Richter, B.; Bensch, W. The Role of Reduced Graphite Oxide in Transition Metal Oxide Nanocomposites Used as Li Anode Material: An Operando Study on $CoFe_2O_4$/RGO. *Chem. - Eur. J.* **2016**, *22*, 16929−16938.
(42) Zhou, D.; Permien, S.; Rana, J.; Krengel, M.; Sun, F.; Schumacher, G.; Bensch, W.; Banhart, J. Investigation of Electronic and Local Structural Changes during Lithium Uptake and Release of Nano-Crystalline $NiFe_2O_4$ by X-Ray Absorption Spectroscopy. *J. Power Sources* **2017**, *342*, 56−63.
(43) Schmidt, P. How to Get Ternary Solid Solutions $Fe_{1-x}M'_xO$ (M = Co, Ni)? A Thermodynamic Concept. *Eur. J. Inorg. Chem.* **2008**, *2008*, 2847−2855.
(44) Armbruster, T. New Solid Solution Series between Rocksalt and Spinel Structure. *Naturwissenschaften* **1977**, *64*, 635−636.
(45) Ma, C.; Gao, H. Preparation and Characterization of Single-Phase $NiMn_2O_4$ NTC Ceramics by Two-Step Sintering Method. *J. Mater. Sci.: Mater. Electron.* **2017**, *28*, 6699−6703.
(46) Savić, S. M.; Mančić, L.; Vojisavljević, K.; Stojanović, G.; Branković, Z.; Aleksić, O. S.; Branković, G. Microstructural and Electrical Changes in Nickel Manganite Powder Induced by Mechanical Activation. *Mater. Res. Bull.* **2011**, *46*, 1065−1071.
(47) Kiziltas-Yavuz, N.; Yavuz, M.; Indris, S.; Bramnik, N. N.; Knapp, M.; Dolotko, O.; Das, B.; Ehrenberg, H.; Bhaskar, A. Enhancement of Electrochemical Performance by Simultaneous Substitution of Ni and Mn with Fe in Ni-Mn Spinel Cathodes for Li-Ion Batteries. *J. Power Sources* **2016**, *327*, 507−518.
(48) Liu, G. Q.; Wen, L.; Wang, X.; Ma, B. Y. Effect of the Impurity $Li_xNi_{1-x}O$ on the Electrochemical Properties of 5 V Cathode Material $LiNi_{0.5}Mn_{1.5}O_4$. *J. Alloys Compd.* **2011**, *509*, 9377−9381.
(49) Feltz, A.; Töpfer, J.; Neidnicht, B. Untersuchungen an elektronenleitenden Oxidsystemen. XXIII. Struktur und Eigenschaften stabiler Spinelle in den Reihen $M_zNiMn_{2-Z}O_4$ (M = Li, Fe). *Z. Anorg. Allg. Chem.* **1993**, *619*, 39−46.

DOI: 10.1021/acsomega.8b03276
ACS Omega 2019, 4, 2398−2409

(50) Roumaih, K.; Manapov, R. A.; Sadykov, E. K.; Pyataev, A. V. Mössbauer Studies of $Cu_{1-x}Ni_xFeMnO_4$ Spinel Ferrites. *J. Magn. Magn. Mater.* **2005**, *288*, 267−275.
(51) Dedryvère, R.; Laruelle, S.; Grugeon, S.; Poizot, P.; Gonbeau, D.; Tarascon, J.-M. Contribution of X-Ray Photoelectron Spectroscopy to the Study of the Electrochemical Reactivity of CoO toward Lithium. *Chem. Mater.* **2004**, *16*, 1056−1061.
(52) Laruelle, S.; Grugeon, S.; Poizot, P.; Dollé, M.; Dupont, L.; Tarascon, J.-M. On the Origin of the Extra Electrochemical Capacity Displayed by MO/Li Cells at Low Potential. *J. Electrochem. Soc.* **2002**, *149*, A627−A634.
(53) Poizot, P.; Laruelle, S.; Grugeon, S.; Dupont, L.; Tarascon, J.-M. Searching for New Anode Materials for the Li-Ion Technology: Time to Deviate from the Usual Path. *J. Power Sources* **2001**, *97*−*98*, 235−239.
(54) Balaya, P.; Li, H.; Kienle, L.; Maier, J. Fully Reversible Homogeneous and Heterogeneous Li Storage in RuO_2 with High Capacity. *Adv. Funct. Mater.* **2003**, *13*, 621−625.
(55) Kuzmin, A.; Chaboy, J. EXAFS and XANES Analysis of Oxides at the Nanoscale. *IUCrJ* **2014**, *1*, 571−589.
(56) Piquer, C.; Laguna-Marco, M. A.; Roca, A. G.; Boada, R.; Guglieri, C.; Chaboy, J. Fe K-Edge X-Ray Absorption Spectroscopy Study of Nanosized Nominal Magnetite. *J. Phys. Chem. C* **2014**, *118*, 1332−1346.
(57) Wang, A.; Kadam, S.; Li, H.; Shi, S.; Qi, Y. Review on Modeling of the Anode Solid Electrolyte Interphase (SEI) for Lithium-Ion Batteries. *npj Comput. Mater.* **2018**, *4*, No. 15.
(58) Hu, Y.-Y.; Liu, Z.; Nam, K.-W.; Borkiewicz, O. J.; Cheng, J.; Hua, X.; Dunstan, M. T.; Yu, X.; Wiaderek, K. M.; Du, L.-S.; Chapman, K. W.; Chupas, P. J.; Yang, X.-Q.; Grey, C. P. Origin of Additional Capacities in Metal Oxide Lithium-Ion Battery Electrodes. *Nat. Mater.* **2013**, *12*, 1130−1136.
(59) Bracamonte, M. V.; Primo, E. N.; Luque, G. L.; Venosta, L.; Bercoff, P. G.; Barraco, D. E. Lithium Dual Uptake Anode Materials: Crystalline Fe_3O_4 Nanoparticles Supported over Graphite for Lithium-Ion Batteries. *Electrochim. Acta* **2017**, *258*, 192−199.
(60) Lowe, M. A.; Gao, J.; Abruña, H. D. In Operando X-Ray Studies of the Conversion Reaction in Mn_3O_4 Lithium Battery Anodes. *J. Mater. Chem. A* **2013**, *1*, 2094−2103.
(61) Cheng, G.; Carter, J. D.; Guo, T. Investigation of Co Nanoparticles with EXAFS and XANES. *Chem. Phys. Lett.* **2004**, *400*, 122−127.
(62) Grey, C. P.; Dupré, N. NMR Studies of Cathode Materials for Lithium-Ion Rechargeable Batteries. *Chem. Rev.* **2004**, *104*, 4493−4512.
(63) Zhan, C.; Lu, J.; Jeremy Kropf, A.; Wu, T.; Jansen, A. N.; Sun, Y.-K.; Qiu, X.; Amine, K. Mn(II) Deposition on Anodes and Its Effects on Capacity Fade in Spinel Lithium Manganate−Carbon Systems. *Nat. Commun.* **2013**, *4*, No. 2437.
(64) Filik, J.; Ashton, A. W.; Chang, P. C. Y.; Chater, P. A.; Day, S. J.; Drakopoulos, M.; Gerring, M. W.; Hart, M. L.; Magdysyuk, O. V.; Michalik, S.; Smith, A.; Tang, C. C.; Terrill, N. J.; Wharmby, M.; Wilhelm, H. Processing Two-Dimensional X-Ray Diffraction and Small-Angle Scattering Data in *DAWN* 2. *J. Appl. Crystallogr.* **2017**, *50*, 959−966.
(65) Yang, X.; Juhas, P.; Farrow, C. L.; Billinge, S. J. L. XPDFsuite: An End-to-End Software Solution for High Throughput Pair Distribution Function Transformation, Visualization and Analysis. 2014, arXiv:1402.3163. arXiv.org e-Printarchive. https://arxiv.org/abs/1402.3163 (accessed Feb 13, 2014).
(66) Juhás, P.; Davis, T.; Farrow, C. L.; Billinge, S. J. L. PDFgetX3: A Rapid and Highly Automatable Program for Processing Powder Diffraction Data into Total Scattering Pair Distribution Functions. *J. Appl. Crystallogr.* **2013**, *46*, 560−566.
(67) Coelho, A. A. *Topas Academic*, version 6; Australia, 2016.
(68) Ravel, B.; Newville, M. ATHENA, ARTEMIS, HEPHAESTUS: Data Analysis for X-Ray Absorption Spectroscopy Using IFEFFIT. *J. Synchrotron Radiat.* **2005**, *12*, 537−541.
(69) Lande, J.; Webb, S. M.; Mehta, A. Area Diffraction Machine, 2008.

DOI: 10.1021/acsomega.8b03276
ACS Omega 2019, 4, 2398−2409